

Manuscript Number: JCOMP-D-13-00928

Title: Discontinuous Finite Element Solution of the Radiation Diffusion Equation on Arbitrary Polygonal Meshes and Locally Adapted Quadrilateral Grids

Article Type: Regular Article

Keywords: Radiation Diffusion; Arbitrary Polygonal Grids; Discontinuous Finite Element; Adaptive Mesh Refinement

Corresponding Author: Dr. Jean C Ragusa, PhD

Corresponding Author's Institution: Texas A&M University

First Author: Jean C Ragusa, PhD

Order of Authors: Jean C Ragusa, PhD

Abstract: In this paper, we propose a piece-wise linear discontinuous (PWLD) finite element discretization of the diffusion equation for arbitrary polygonal meshes. It is based on the standard diffusion form and uses the symmetric interior penalty technique, which yields a symmetric positive definite linear system matrix. A preconditioned conjugate gradient algorithm is employed to solve the linear system.

Piece-wise linear approximations also allow a straightforward implementation of local mesh adaptation by allowing unrefined cells to be interpreted as polygons with an increased number of vertices.

Several test cases, taken from the literature on the discretization of the radiation diffusion, are presented: random, sinusoidal, Shestakov, and Z meshes are used. The last numerical example demonstrates the application of the PWLD discretization to adaptive mesh refinement.

Suggested Reviewers: Todd Palmer PhD
Professor, Nuclear engineering, Oregon State University
palmerts@engr.orst.edu
expert in radiation transport;

has worked on the discretization of the diffusion equation on polygonal meshes (references 2 and 9 cited in our manuscript)

Teresa Bailey PhD
research scientist, LLNL
bailey42@llnl.gov
has developed a piece-wise linear continuous FEM solution technique of the diffusion equation for polygonal/polyhedral grids (published in JCP in 2008)

has worked on the discretization of the diffusion equation on polygonal meshes (references 6, 7, and 21 cited in our manuscript)

expert in radiation transport;

Jim Morel PhD

Professor, Nuclear engineering, Texas A&M university

morel@tamu.edu

expert in radiation transport;

has worked on the discretization of the diffusion equation on polygonal meshes, developing the mimetic finite difference technique (references 10, 11, 12, 17, 18, and 33 cited in our manuscript)

Mikhail Shashkov PhD

research scientist, XCP-4 Methods and Algorithms, LANL

shashkov@lanl.gov

expert in radiation transport;

has worked on the discretization of the diffusion equation on polygonal meshes, developing the mimetic finite difference technique (references 3, 5, 8, 10, 11, 12 and 38 cited in our manuscript)

Jean Ragusa
Department of Nuclear Engineering
Texas A&M University
College Station, TX 77843-3133, USA
phone: (979) 862 2033
e-mail: jean.ragusa@tamu.edu

August 13, 2013

Professor William Martin
Editor,
Journal of Computational Physics

Dear Professor Martin,

Please find attached a copy of our manuscript titled “Discontinuous Finite Element Solution of the Radiation Diffusion Equation on Arbitrary Polygonal Meshes and Locally Adapted Quadrilateral Grids” for submission to the *Journal of Computational Physics*.

In this paper, we propose a piecewise linear *discontinuous* finite element discretization of the standard diffusion equation for arbitrary polygonal grids.

This work follows closely prior works by Jim Morel (LANL, now TAMU), Mikhail Shashkov (LANL), Teresa Bailey (LLNL), Marvin Adams (TAMU), and Todd Palmer (OSU).

Our work is based on the standard diffusion form and uses the symmetric interior penalty technique, which yields a symmetric positive definite linear system matrix. A preconditioned conjugate gradient algorithm is employed to solve the linear system. Piecewise linear approximations also allow a straightforward implementation of local mesh adaptation by allowing unrefined cells to be interpreted as polygons with an increased number of vertices. Several test cases, taken from the literature on discretizations of the radiation diffusion, are presented: random, sinusoidal, Shestakov, and Z meshes are used. The last numerical example demonstrates the application of the PWLD discretization to adaptive mesh refinement.

Employing a DFEM approximation to solve the diffusion equation is not commonly done (especially on polygonal grids), but this will allow us to use proven DFEM-based DSA preconditioners to tackle radiation transport problems on polygonal grids in the future.

Thank you for considering this manuscript for publication in JCP.

Best regards,

Jean Ragusa

Discontinuous Finite Element Solution of the Radiation Diffusion Equation on Arbitrary Polygonal Meshes and Locally Adapted Quadrilateral Grids

Jean C. Ragusa

Department of Nuclear Engineering, Texas A&M University, College Station, TX 77843, USA

Abstract

In this paper, we propose a piece-wise linear discontinuous (PWLD) finite element discretization of the diffusion equation for arbitrary polygonal meshes. It is based on the standard diffusion form and uses the symmetric interior penalty technique, which yields a symmetric positive definite linear system matrix. A preconditioned conjugate gradient algorithm is employed to solve the linear system. Piece-wise linear approximations also allow a straightforward implementation of local mesh adaptation by allowing unrefined cells to be interpreted as polygons with an increased number of vertices. Several test cases, taken from the literature on the discretization of the radiation diffusion, are presented: random, sinusoidal, Shestakov, and Z meshes are used. The last numerical example demonstrates the application of the PWLD discretization to adaptive mesh refinement.

Key words: Radiation Diffusion, Arbitrary Polygonal Grids, Discontinuous Finite Element, Adaptive Mesh Refinement

1. Introduction

This paper deals with a Piece-Wise Linear Discontinuous (PWLD) finite element spatial discretization of the radiation diffusion equation on arbitrary polygonal grids, with and without adaptive mesh refinement. Radiation diffusion is an asymptotic limit of the radiation transport equation and can be written in the following form:

$$-\vec{\nabla} \cdot D(\vec{r}) \vec{\nabla} E(\vec{r}) + \sigma_a(\vec{r}) E(\vec{r}) = Q(\vec{r}), \quad (1)$$

where E is the radiation energy intensity, D is a diffusion coefficient, σ_a is an opacity coefficient, and Q is the source.

Email address: jean.ragusa@tamu.edu (Jean C. Ragusa)

9 Several spatial discretizations have been proposed to solve Eq. (1) on ar-
 10 bitrary polygons (2D) and polyhedra (3D) [1, 2, 3, 4, 5, 6, 7, 8]. We review
 11 them below. Wachspress [1] developed a family of rational polynomial func-
 12 tions that can be employed as basis functions in a finite element method on
 13 polygonal/polyhedral grids. This yields symmetric positive-definite (SPD) ma-
 14 trices but (i) the finite element integrals must be carried out numerically and
 15 (ii) the Jacobian of the transformation becomes zero on degenerate cells (such
 16 as the ones shown on Fig. 1) and on non-convex cells. Palmer [2, 9] proposed
 17 a node-based finite volume method that enforces particle balance over the con-
 18 trol volume associated with a given grid vertex. This control volume defines a
 19 dual cell constructed as the union of all corners surrounding the specified vertex
 20 v . In 2D, a corner is a quadrilateral with the following vertices: vertex p , the
 21 cell center, and the midpoint of the edges that contain vertex p . On a trian-
 22 gular grid, Palmer’s scheme is equivalent to employing linear continuous finite
 23 elements with “mass-matrix lumping”. This method is second-order accurate
 24 but its discretization of the diffusion equation produces an asymmetric (i.e.,
 25 not SPD) matrix, in general. Mimetic finite difference methods create discrete
 26 analog of vector and tensor calculus in order to accurately approximate the orig-
 27 inal differential operators; see, e.g., [10]. Mimetic methods preserve important
 28 properties of the differential operators such as symmetry, positivity, monotonic-
 29 ity, asymptotic limits, and identities pertaining to tensor and vector calculus.
 30 Mimetic methods can also be viewed as mixed hybrid finite element formulations
 31 with specific spatial quadratures. In addition to quadrilateral and hexahedral
 32 meshes (see, e.g., [11, 12], mimetic finite difference methods have recently been
 33 applied to the diffusion equation on arbitrary polygonal grids [3, 4, 5, 8]. Bailey
 34 et al. [7] recently employed piece-wise linear basis functions to solve a diffusion
 35 equation using a Galerkin finite element technique on arbitrary polygonal and
 36 polyhedral grids. Their goal was to devise a *continuous* finite element discretiza-
 37 tion that does not necessitate numerical integration, yields an SPD matrix, is
 38 second-order accurate, and handles arbitrary polygonal/polyhedral grids (in-
 39 cluding grids with degenerate cells). The approach they followed is a standard
 40 Galerkin weak formulation for continuous finite elements, with piece-wise lin-
 41 ear basis functions defined on subcells (which they called “sides”) of arbitrary
 42 polygons/polyhedrons.

43 In this paper, we are interested in solving a diffusion equation on arbitrary
 44 polygonal grids using a *discontinuous* finite element discretization. We employ
 45 the Symmetric Interior Penalty (SIP) technique [13, 14, 15], developed for the
 46 discretization of elliptic equations using discontinuous Galerkin techniques; this
 47 results in a linear system matrix that is Symmetric Positive Definite (SPD). For
 48 basis functions, we use the piece-wise linear functions of [7]. The motivations
 49 for employing discontinuous finite elements on polygonal grids are as follows:

- 50 1. prior works dealing with the spatial discretization of the radiation diffu-
 51 sion equation on polygonal meshes have used finite volume, mimetic finite
 52 differences, and continuous finite element techniques; we wish to test the
 53 performance of Piece-Wise linear discontinuous finite elements for such

54 grids;

- 55 2. prior works also dealt with spatial discretization errors on highly distorted
56 quadrilateral grids; we wish to assess the accuracy of a PWLD discretiza-
57 tion on such grids as well;
- 58 3. a diffusion solve often serves as a synthetic accelerator or preconditioner
59 for iterative solution techniques applied to radiation transport problems
60 [16, 17]. On unstructured and polygonal/polyhedral grids, a discontinu-
61 ous finite element technique is often employed to discretize the transport
62 equation [18, 19, 20, 21, 22]; it was found in [23] that employing the same
63 discretization technique for both the radiation transport solve and its dif-
64 fusion preconditioner was effective on triangular grids. In developing a
65 PWLD-based diffusion preconditioner for transport solves, one needs to
66 evaluate the effectiveness of a PWLD discretization of the diffusion equa-
67 tion first.
- 68 4. It has been proposed that PWL continuous discretizations can more seam-
69 lessly handle locally refined grids as produced by Adaptive Mesh Refine-
70 ment (AMR) algorithms [7]. In [7], the authors generated a grid with two
71 refinement levels and for a problem with a linear solution. Here, we fully
72 embed a PWL discontinuous discretization in an AMR process and test it
73 with more complex solutions.

74 The remainder of the paper is as follows. In Section 2, we further discuss the
75 use of polygonal meshes, define the piece-wise linear discontinuous basis func-
76 tions for arbitrary polygons, and examine how polygonal grids can be utilized
77 in handling local mesh refinement (as in AMR approaches). The Symmetric
78 Interior Penalty technique applied to the diffusion equation is reviewed in Sec-
79 tion 3. Mesh adaptivity utilizing piece-wise linear basis function is presented
80 in Section 4. Results are provided in Section 5; all of the test cases presented
81 here are borrowed from the literature on spatial discretization techniques ap-
82 plied to the diffusion equation solved on highly distorted quadrilateral grids and
83 polygonal grids.

84 2. Polygonal Grids and Piece-wise Linear Basis Functions

85 2.1. Polygonal Meshes and their Application to Adaptive Mesh Refinement

86 Polygonal cells are an alternative to standard (triangles/quads) mesh par-
87 titioning. Mesh generation using polygons (polyhedra in 3D) is an active area
88 of research. Some meshing tools, such as MSTK [24] and the Computational
89 Geometry Algorithms Library [25, 26], may be employed to generate/process
90 polygonal meshes. Several CFD codes (Fluent, StarCCM, OpenFoam) also offer
91 polygonal meshing and solver capabilities. The rationale for polygonal/polyhedral
92 cells is as follows. While quadrilaterals (hexahedra in 3D) can be seen as the
93 standard cell shapes for logically structured meshes, they may be difficult to
94 employ in complex geometries. For unstructured meshes, triangles (tetrahedra
95 in 3D) are the typical building blocks and are employed in numerous automated
96 meshing algorithms, but are not well-suited for boundary layers, for instance,

97 and may require higher cell counts than quad/hex meshes for a similar resolu-
 98 tion. The following features of polygonal cells are noteworthy:

- 99 • They can provide a better partition of the domain, minimizing the bound-
 100 ary/interior ratio;
- 101 • The number of unknowns for an equivalent accuracy/resolution can be
 102 reduced (similar to the advantages of hex meshes over tet meshes);
- 103 • The notion of transition elements is included by default in arbitrary grids
 104 composed of polygons/polyhedra. Therefore, such a grid can easily be
 105 split by cut planes, for instance.
- 106 • The notion of “hanging nodes” for locally refined/adapted meshed is no
 107 longer needed. For example, Fig. 1(a) shows two quadrilateral elements
 108 before local refinement; on Fig. 1(b), one of the two cells has been refined.
 109 The un-refined cell can now be viewed as a pentagon.

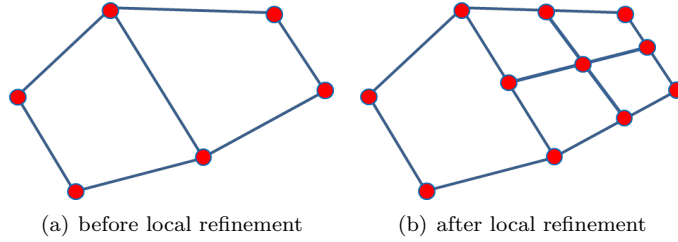


Figure 1: Local mesh refinement leads to pentagonal cell

110 2.2. Piece-wise Linear Basis Functions on Arbitrary Polygons

111 Here, we describe piece-wise linear finite elements basis functions for arbi-
 112 trary polygons. Consider a polygonal cell with N_V vertices, (x_i, y_i) for $1 \leq i \leq$
 113 N_V . The polygon needs not to be convex. In order to describe the piece-wise
 114 linear basis functions for such a cell, we introduce a cell “center”, denoted here-
 115 after by $c = (x_c, y_c)$, with $x_c = \sum_{i=1}^{N_V} \alpha_i x_i$ and $y_c = \sum_{i=1}^{N_V} \alpha_i y_i$. We require that
 116 $\sum_{i=1}^{N_V} \alpha_i = 1$. Thus, point c can be interpreted as a weighted average of the
 117 polygon’s vertices. Often, one chooses $\alpha_i = 1/N_V$ but one may also define point
 118 c as the centroid of the polygon under consideration. With the introduction of
 119 the cell center, the polygon can also be described as N_V triangular subcells (or
 120 “sides” if using the terminology of [7]), with each of these triangles being com-
 121 posed of two successive vertices and the cell center. The N_V piece-wise linear
 122 basis functions are then given by:

$$b_i(\mathbf{r}) = t_i(\mathbf{r}) + \alpha_i t_c(\mathbf{r}), \quad i = 1, \dots, N_V, \quad (2)$$

123 where $t_i(\mathbf{r})$ is the standard linear function defined on the two adjacent triangular
 124 subcells formed by (1) vertex i , vertex $i - 1$ and the cell center c , and (2) vertex

125 i , vertex $i + 1$ and the cell center c . t_i is equal to one at the i^{th} vertex and
 126 to zero at all other vertices of the polygon, as well as at the cell center. $t_c(\mathbf{r})$
 127 is the “tent” function associated with the cell center and is equal to one at
 128 the cell center and to zero at all of the polygon vertices. We stress that this
 129 choice of basis functions is not equivalent to employing a standard continuous
 130 finite element representation within a polygon. Indeed, in the case of a standard
 131 continuous finite element representation, the number of basis functions would
 132 be equal to $N_V + 1$ (for the N_V vertices and the cell center). In the piece-wise
 133 linear representation, the unknowns are only located at the cell vertices and the
 134 cell center point is only used to define the basis functions. For example, Fig. 2
 135 presents two simple examples of polygonal cells: a pentagon and a degenerated
 136 pentagon, the later is typically obtained during local mesh adaptation (see also
 137 Fig. 1(b)). The isolines of the piece-wise linear basis functions for vertex D and
 138 E are graphed in Fig. 3 for the regular pentagon and in Fig. 4 for the degenerate

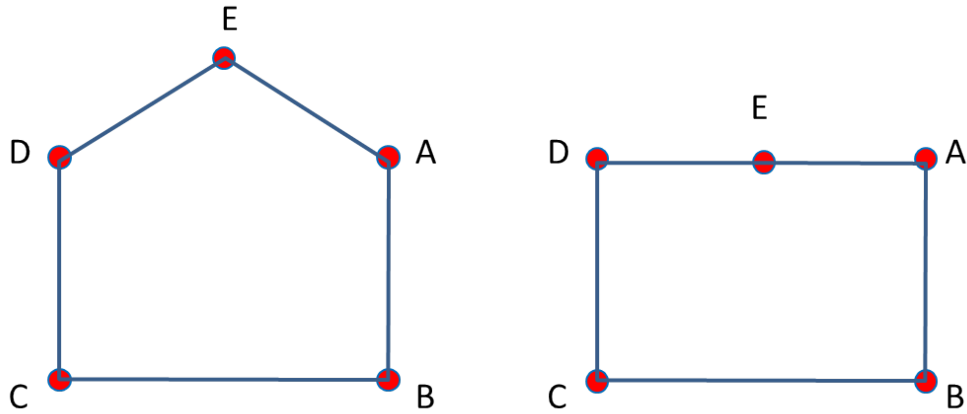


Figure 2: Non-degenerate (left) and degenerate (right) pentagonal cells

140 3. Discontinuous Finite Element Formulation

141 In this Section, we present the discontinuous Galerkin finite element tech-
 142 nique employed to discretize the radiation diffusion equation on arbitrary polyg-
 143 onal grids. Many variants of such discontinuous discretization methods exist for
 144 diffusion problems (depending, for instance, on the choice of stabilization terms,
 145 whether the diffusion equation is expressed in its mixed form, ...). We refer
 146 the Readers to the review paper [14] for additional details. Here, we employ the
 147 Symmetric Interior Penalty (SIP) method which we have found to be robust in
 148 our test cases and relatively simple to implement. The general idea of interior
 149 penalty methods can be traced back to [27], where the Dirichlet boundary con-
 150 ditions to the model diffusion problem $\{-\vec{\nabla} \cdot \vec{\nabla} E = Q$ in domain \mathcal{D} , $E = E^d$ on

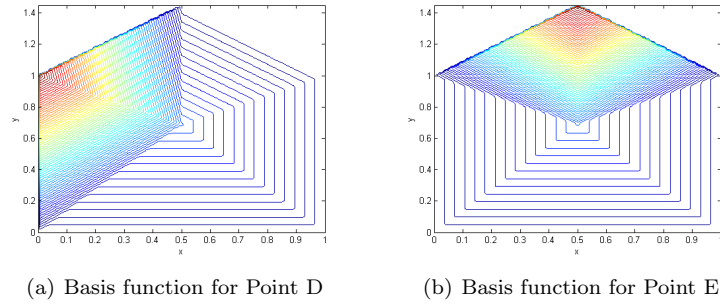


Figure 3: Isolines of PWL basis functions for a non-degenerate pentagon

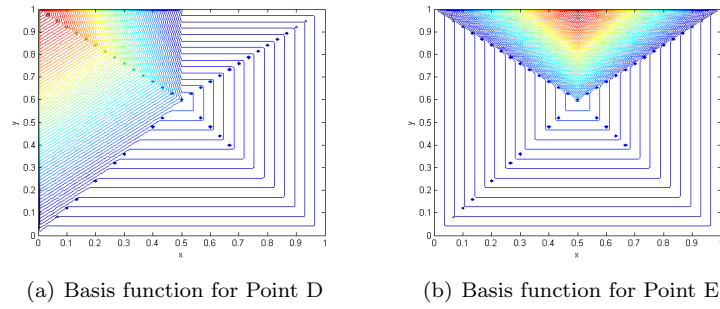


Figure 4: Isolines of PWL basis functions for a degenerate pentagon

the boundary $\partial\mathcal{D}$ have been enforced via a penalty method, thereby modifying the boundary condition to read $E + \frac{1}{\mu}\partial_n E = E^d$ with $\mu \gg 1$. Later, Nitsche [28] proposed a consistent formulation for the enforcement of the Dirichlet boundary condition with a penalty term, leading to the weak formulation:

$$\int_{\mathcal{D}} \vec{\nabla} E \cdot \vec{\nabla} b - \int_{\partial\mathcal{D}} \partial_n E b - \int_{\partial\mathcal{D}} \partial_n b E + \int_{\partial\mathcal{D}} \mu(E - E^d)b = \int_{\mathcal{D}} Qb - \int_{\partial\mathcal{D}} E^d \partial_n b, \quad (3)$$

with b a finite element basis function and $\mu = \alpha/h$, where h denotes the mesh size and $\alpha > 1$ is a constant. Nitsche's idea, extended to all cell edges (not only cells with edges on the boundary), leads to the family of interior penalty methods for discontinuous finite elements. The SIP form, which we have chosen here because it is one of the simplest forms and leads to symmetric positive definite matrices, is discussed next. But first, we recall Eq. (1) and specify Dirichlet, Neumann, and Robin boundary condition types on various portions of the domain's boundary: the radiation diffusion equation is given by

$$-\vec{\nabla} \cdot D(\vec{r}) \vec{\nabla} E(\vec{r}) + \sigma_a(\vec{r}) E(\vec{r}) = Q(\vec{r}) \quad \text{for } \vec{r} \in \mathcal{D}, \quad (4)$$

with Dirichlet boundary conditions

$$E(\vec{r}) = E_0(\vec{r}) \quad \text{for } \vec{r} \in \partial\mathcal{D}^d, \quad (5)$$

Neumann boundary conditions

$$-D\partial_n E(\vec{r}) = F_0(\vec{r}) \quad \text{for } \vec{r} \in \partial\mathcal{D}^n, \quad (6)$$

and Robin boundary conditions

$$\frac{1}{4}E(\vec{r}) + \frac{1}{2}D(\vec{r})\partial_n E(\vec{r}) = F^{inc}(\vec{r}) \quad \text{for } \vec{r} \in \partial\mathcal{D}^r. \quad (7)$$

E is the unknown radiation scalar intensity. The boundary of the domain is split such that $\partial\mathcal{D} = \partial\mathcal{D}^d \cup \partial\mathcal{D}^n \cup \partial\mathcal{D}^r$, where the superscripts denote Dirichlet, Neumann, and Robin types, respectively. E_0 , F_0 , and F^{inc} are specified quantities. $\partial_n \square$ denotes $\vec{\nabla} \square \cdot \vec{n}$ with \vec{n} the outward unit normal vector.

3.1. The Symmetric Interior Penalty (SIP) Method

In this paragraph, we describe the SIP discretization [14, 15] applied to the radiation diffusion equation using discontinuous finite elements. We introduce a partition of the domain, $\bigcup_{K \in \mathbb{T}_h} K = \mathcal{D}$, and also assume that the boundary of the domain, $\partial\mathcal{D}$, consists of straight edges only. The set of interior and boundary edges is denoted by \mathcal{E}_h^i and $\mathcal{E}_h^{\partial\mathcal{D}}$, respectively; the set of boundary edges is further split into the three different boundary condition types, i.e.,

$\mathcal{E}_h^{\partial\mathcal{D}} = \mathcal{E}_h^{\partial\mathcal{D}^d} \cup \mathcal{E}_h^{\partial\mathcal{D}^n} \cup \mathcal{E}_h^{\partial\mathcal{D}^r}$. Then, the SIP formulation is given by

$$\begin{aligned} & \int_{\mathbb{T}_h} \left(D \vec{\nabla} E \cdot \vec{\nabla} b + \sigma_a E b \right) + \int_{\mathcal{E}_h^i} \left(\llbracket D \partial_n E \rrbracket \llbracket b \rrbracket + \llbracket D \partial_n b \rrbracket \llbracket E \rrbracket + \kappa \llbracket E \rrbracket \llbracket b \rrbracket \right) \\ & + \int_{\mathcal{E}_h^{\partial\mathcal{D}^d}} \left(\kappa E b - D b \partial_n E - D E \partial_n b \right) + \frac{1}{2} \int_{\mathcal{E}_h^{\partial\mathcal{D}^r}} E b \\ & = \int_{\mathbb{T}_h} Q b + \int_{\mathcal{E}_h^{\partial\mathcal{D}^d}} E_0 \left(\kappa b - D \partial_n b \right) - \int_{\mathcal{E}_h^{\partial\mathcal{D}^n}} F_0 b + \int_{\mathcal{E}_h^{\partial\mathcal{D}^r}} 2 F^{inc} b, \quad (8) \end{aligned}$$

where we recall that b is a generic test function. In Eq. (8), the last term on the left-hand side and the last two terms on the right-hand side are naturally obtained by applying the Neumann and Robin boundary conditions. The terms pertaining to the Dirichlet boundary conditions are identical to the ones of Nitsche's penalty method. Finally, the interior edge terms are the standard terms due to the extension of Nitsche's method to the interior edges. To generate the linear system associated with Eq. (8), we have opted to use two loops: one over the elements to compute the volume integrals,

$$\int_{\mathbb{T}_h} \longrightarrow \sum_{K \in \mathbb{T}_h} \int_K, \quad (9)$$

and one of the edge sets to compute the edge integrals

$$\int_{\mathcal{E}_h} \longrightarrow \sum_{e \in \mathcal{E}_h} \int_e. \quad (10)$$

We have also chosen to arbitrarily assign a unit normal vector, \vec{n} , to each interior edge (for the boundary edges, \vec{n} is always to outward point unit normal vector). With this choice, the definition of the mean value and the jump of a quantity u on any given interior edge are given by

$$\llbracket u \rrbracket = \frac{u^+ + u^-}{2} \quad (11)$$

and

$$\llbracket u \rrbracket = u^+ - u^-, \quad (12)$$

respectively. The values taken by the quantity u while approaching the edge from either one of its sides are defined as follows:

$$u^\pm = \lim_{s \rightarrow 0^\pm} u(\vec{r} + s \vec{n}), \quad (13)$$

for any point \vec{r} on that edge (that is, u^+ is the trace of u along that edge taken from the cell pointed by \vec{n}). The penalty coefficient, κ , is edge-dependent and is given by

$$\kappa_e = \begin{cases} \frac{C}{2} \left(\frac{D^+}{h_\perp^+} + \frac{D^-}{h_\perp^-} \right) & \text{for interior edges, i.e., } e \in \mathcal{E}_h^i, \\ 2C \frac{D^-}{h_\perp^-} & \text{for boundary edges, i.e., } e \in \partial\mathcal{E}_h^{\partial\mathcal{D}} \end{cases}, \quad (14)$$

where C is a constant, h_{\perp} is the length of the cell in the direction orthogonal to edge e . For quadrilateral meshes with linear basis functions, researchers typically utilize $C \geq 4$ (through the formula $C = c(p+1)^2$, with $c \geq 1$ and p the polynomial order). Here, we use $C = 4$. For boundary edges, Kanschat [15] noted that doubling the value of C (on quadrilateral meshes) was beneficial; we have followed their recommendations. In Eq. (14), the \pm superscripts represent again values taken from either side of an edge. For triangular cells, h_{\perp} is exactly given by $h_{\perp} = \frac{2A}{L_e}$ where A is the triangle area and L_e is the length of edge e . However, there are no formulae to compute h_{\perp} for arbitrary polygons. In [29], polygonal cells were assumed to be regular polygonal cells, in which case h_{\perp}^{reg} is given by twice the inradius for regular even-sided polygons and by the inradius plus the circumradius for odd-sided polygons. The inradius and the circumradius are computed using the area and perimeter of the actual polygonal cell.

4. Adaptive Mesh Refinement Using PWLD Basis Functions

Solutions with strong and rapid spatial variations can be accurately captured using mesh adaptivity [30]. Adaptive Mesh Refinement (AMR) techniques require local error estimates to determine which cells to refine. When using discontinuous finite elements, the numerical solution is discontinuous across the edges (faces in 3D) between neighboring cells. The magnitude of these jumps is small in regions where the solution is smooth and can be significantly larger in regions where the solution undergoes rapid spatial variations. A heuristic local error indicator is, therefore, to monitor the interfacial jumps. Following [31, 22], we define the error indicator on cell K as:

$$\eta_K = \frac{\int_{\partial K} |[E]|_{\partial K}}{\text{meas}(\partial K)}. \quad (15)$$

The cells flagged for refinement are such that

$$\eta_K \geq \theta \max_{K' \in \mathbb{T}_h} (\eta_{K'}), \quad (16)$$

where $0 \leq \theta \leq 1$ is a user-specified coefficient. Eq. (16) signifies that cells selected for refinement are such that their error, normalized to the largest error, is larger than or equal to θ .

As noted in the Introduction, piece-wise linear basis functions can be beneficially used to handle transitions between mesh cells of different refinement levels. In the context of discontinuous finite elements, the analog of Fig. 1 is shown in Fig. 5. With standard linear discontinuous finite element representation, the cell that will not undergo refinement (labeled K in Fig. 5(a)) would remain a quadrilateral after refinement of its neighbor, cell K' ; with such a representation, the restriction of the intensity along edge AB of cell K would remain a linear function. However, when employing PWLD basis functions, cell K becomes a pentagon after refinement of its neighbor and the restriction of

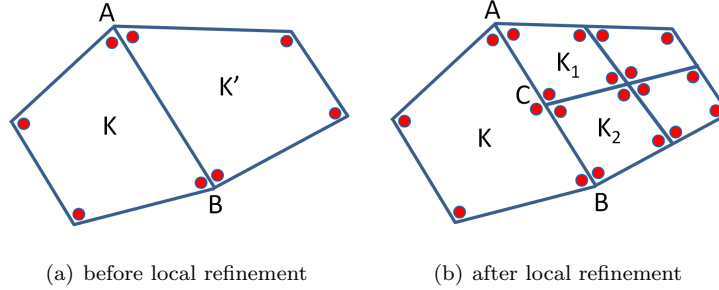


Figure 5: Local mesh refinement using piece-wise linear discontinuous basis functions

the intensity along the “degenerate” edge AB of that pentagon now becomes piece-wise linear.

In this work, we only consider the application of piece-wise linear functions to AMR for grids that are initially composed of quadrilateral cells only and refine cells flagged for adaptivity by subdividing them into four children cells; the child cell contains the following four vertices: one of the corners of its parent cell, the midpoint of the two edges that contain that corner, and the centroid of the parent cell. For simplicity in the refinement process, we also limit the refinement level differences between neighboring cells to one, but stress that this is not at all a limitation of PWLD functions. Furthermore, with standard finite element representations, one often imposes refinement of a cell when three or more of its neighbors at the same refinement depth have already been further refined (known as Bank’s k -neighbor rule, [32]). Such a situation would arise for a quadrilateral cell when at least three of its four neighbors have been refined, then, according to Bank’s rule, that quadrangle would also have to be refined. However, with PWLD functions, such a cell is viewed as a heptagon (three of its neighbors have been refined) with seven unknowns located at the heptagon’s vertices or as an octagon (all four neighbors have been refined) with eight unknowns.

5. Numerical Results

Solution techniques that preserve linear solutions, are second-order accurate, and do not suffer excessively from a mesh imprint (especially when using highly distorted grids) have been a topic of research in numerous publications dealing with the discretization of the the radiation diffusion equation . Our numerical examples are taken from that literature. Earlier works focused on quadrilateral (and hexahedral) grids [33, 11, 12, 2] and, therefore, we also provide results obtained using four types of quadrilateral meshes used in those publications:

1. “random” grids, obtained by displacing interior vertices of a uniform orthogonal grid by a fraction of the original cell width: $\pm\xi\delta x$ along the x -axis and $\pm\xi\delta y$ along the y -axis, where $\delta x, \delta y$ is the grid resolution and

257 ξ is a random number ($0 \leq \xi \leq 1$). $\xi = 0$ returns the original rectangular
 258 grid. In the literature, a value of ξ in the order of 0.25 or less is often
 259 employed; here we show results with ξ up to 0.65. Above 0.65, some of
 260 the original cells are often flipped onto themselves.

2. “sinusoidal” grids, given by the transformation

$$\begin{aligned} x_{i,j} &= \hat{x}_i + \zeta L_x \sin(2\pi \hat{x}_i / L_x) \sin(2\pi \hat{y}_i / L_y) \\ y_{i,j} &= \hat{y}_i + \zeta L_y \sin(2\pi \hat{x}_i / L_x) \sin(2\pi \hat{y}_i / L_y) \end{aligned}$$

261 with (\hat{x}_i, \hat{y}_i) the vertices of a uniform orthogonal grid over the rectangular
 262 domain $[0, L_x] \times [0, L_y]$, and ζ a distortion parameter ($0 \leq \zeta \leq 1/(2\pi)$).
 263 A rectangular mesh is recovered when $\zeta = 0$. ζ is user-specified and not
 264 randomly generated.

- 265 3. Kershaw’s “Z-mesh” [34]. For Z-meshes, the skewness parameter s varies
 266 between 0 (extremely skewed) and 0.5 (structured rectangular) but note
 267 that here, s is user-specified and not randomly generated.
- 268 4. “Shestakov” grids (due to Shestakov & Kershaw, [35, 36]). For Shes-
 269 takov meshes, the randomness parameter a varies between 0 (extremely
 270 distorted) and 0.5 (structured rectangular).

271 The Z- and Shestakov meshes are meant to model grid distortions that occur in
 272 Lagrangian hydrodynamic simulations.

273 Our examples using polygonal grids are also taken from the current litera-
 274 ture [3, 4, 7]. The polygonal grids employed here are generated by computing a
 275 bounded Voronoi diagram, using the vertices generated from one of the previ-
 276 ous quadrilateral meshes (either the random, sinusoidal, Z-mesh, or Shestakov
 277 quadrilateral grids). The Voronoi diagram is bounded to the size of the original
 278 quadrilateral mesh.

279 The discrete linear system of equation is solved using a preconditioned con-
 280 jugate gradient (PCG) algorithm. SSOR and aggregation Algebraic MultiGrid
 281 [37] are used as preconditioner. A reduction of the initial residual norm by a
 282 factor of 10^{10} is used as the stopping criterion for PCG.

283 5.1. A Standard Problem with Linear Exact Solution

A standard test problem to verify that a numerical scheme preserves lin-
 ear solutions has been proposed by Morel et al. [33]. This test consists in
 solving the radiation diffusion equation on a rectangular domain containing an
 homogeneous pure scatterer material ($\sigma_a = 0$), no volumetric sources ($Q = 0$),
 with reflective boundary conditions on the top and bottom faces, and Robin
 boundary conditions on the left and right faces

$$E(0) - 2D \partial_x E|_0 = 4F^{inc} \forall y \text{ at } x = 0, \quad (17)$$

$$E(L_x) + 2D \partial_x E|_{L_x} = 0 \forall y \text{ at } x = L_x. \quad (18)$$

284 The exact solution (for a domain of length L_x in the x -direction) is

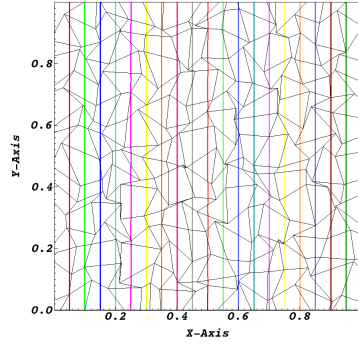
$$E(x, y) = \frac{4F^{inc}}{L_x + 4D} (L_x + 2D - x) \quad (19)$$

Fig. 6 presents the isolines obtained for this problems using four different quadrilateral grids: (a) a 16×16 random grid obtained by randomly moving the vertices of a rectangular grids by 66% ($\alpha = 0.66$), (b) a 20×20 Z-mesh with a skewness factor of $s = 0.05$ (recall that for Z-meshes, skewness increases as $s \rightarrow 0$), (c) a 16×16 Shestakov grid with a randomness factor of $a = 0.15$ (recall also that for Shestakov meshes, randomness increases as $a \rightarrow 0$), and (d) a small 3×3 non-convex grid due to Shashkov [38]. Table 1 summarizes the numbers of non-convex quadrilaterals in each of these grids. For instance, the randomized rectangular grid with $\alpha = 0.66$ contains about 21% of non-convex cells. The linearity of the true solution is exactly reproduced by the piece-wise linear discontinuous finite element solution. In the example chosen ($L = 1, D = 2, F^{inc} = 9$), the solution varies from 20 (left) to 16 (right). Each isoline on the plots represents an increment of 0.2 in the solution.

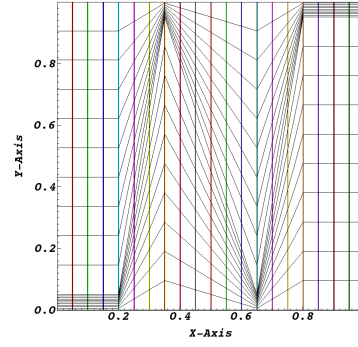
Fig. 7 presents solutions obtained using polygonal grids; the polygonal grids are based on their quadrilateral equivalents, that is, the vertices of a given type of quadrilateral grids are utilized to generate a bounded Voronoi digram. Hence, we still refer to the polygonal meshes as random mesh, Z-mesh, and Shestakov mesh. For instance, one can note that the polygonal versions of the Z-mesh and the Shestakov mesh still contain some feature of their quadrilateral-equivalent. Table 2 summarizes the types and number of polygonal cells found in each of these grids. For example, there are six polygons with 11 sides in the Z-mesh of Fig. 7. The percentages of cells that are not triangular nor quadrangular for the random, Z-mesh, and Shestakov polygonal grids of Fig. 7 are 81%, 48%, and 73%, respectively. As with quadrilateral grids, the linearity of the true solution is exactly reproduced by the piece-wise linear discontinuous finite element solution on polygonal grids.

Grid of Fig. 6	# of convex cells / total # of cells
Random	54 / 256
Z-mesh	0 / 400
Shestakov	22 / 256
Shaskov	4 / 9

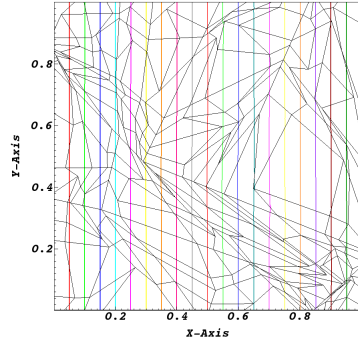
Table 1: Fraction of Concave Cells in Quadrilaterals Grids shown in Fig. 6



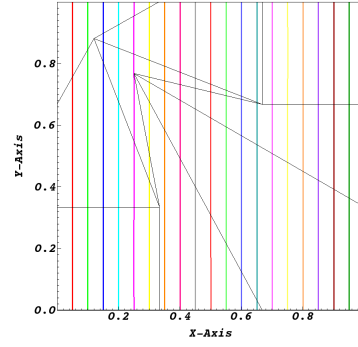
(a) Random quads, $\alpha = 0.66$



(b) Z-mesh, $s = 0.05$

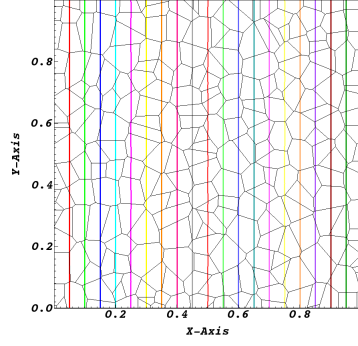


(c) Shestakov, $a = 0.15$

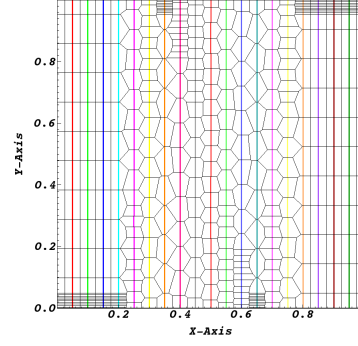


(d) Shaskov 3×3 mesh

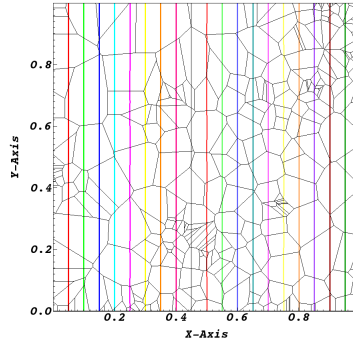
Figure 6: Linear solutions on quadrilateral grids



(a) Random polygons



(b) Z-mesh



(c) Shestakov mesh

Figure 7: Linear solution on polygonal grids

Polygon type	Random	Z-mesh	Shestakov
Triangle	5	0	12
Quadrangle	43	228	65
Pentagon	73	72	83
Hexagon	67	81	50
Heptagon	41	48	36
Octagon	23	2	21
Nonagon	4	4	18
Decagon	0	0	2
Hendecagon	0	6	2

Table 2: Number and type of polygonal cells shown in Fig. 7

311 5.2. Convergence Rate Studies On Distorted Meshes

312 In this example, we compare the convergence rates of PWLD finite elements
313 on several quadrilateral and polygonal meshes using the method of manufact-
314 ures solutions [39]. Using the following exact solution,

$$E^{exa}(x, y) = \sin(\nu\pi x/L_x) \sin(\nu\pi y/L_y) \quad \text{in } \mathcal{D} = [0, L_x] \times [0, L_y] \quad (20)$$

315 with zero-Dirichlet boundary conditions, $D = 1/6$, $\sigma_a = 1$, and ν , a frequency
316 parameter, chosen to be 3 here, one can compute the corresponding volumetric
317 source term $Q(x, y)$ for the diffusion equation. Then, by solving Eq. (1) on a
318 sequence of grids with increasing resolution, one can determine the convergence
319 rate of the error as a function of the number of unknowns. The L_2 -norm of the
320 error, ε_h , is defined in the usual manner:

$$\varepsilon_h^2 = \|E^{exa} - E_h\|_{\mathcal{D}}^2 = \int_{\mathcal{D}} [E^{exa}(x, y) - E_h(x, y)]^2 dx dy. \quad (21)$$

321 To compute with high accuracy the integral of a generic function f on an arbi-
322 trary polygonal partition \mathbb{T}_h of \mathcal{D} , we sum the integration over each polygonal
323 cell; the integration over each cell is split into its triangular sides (using two
324 consecutive vertices and the cell center point); finally, the integration over each
325 triangular side is performed by subdividing each triangle into three quadrangles
326 for which a high-order standard 2D Gauss-Legendre quadrature is used. This
327 can be summarized as follows:

$$\int_{\mathbb{T}_h} f = \sum_{K \in \mathbb{T}_h} \sum_{\text{sides of } K} \sum_{k=1}^3 \sum_{q=1}^{N_q} w_q f_q. \quad (22)$$

328 Note that the same process (subdivision of K into sides that are further split
329 into quadrangles) is also employed to compute accurately the contribution of
330 the volumetric source to the system's right-hand side, $\int_K b_i Q$.

331 For uniform structured meshes, it is fairly straightforward to obtain the
332 asymptotic convergence rate by plotting the error ε_h versus the mesh size h .
333 Conversely, grid resolution is also related to the number of degrees of freedom,
334 N_{dof} (unknowns) via

$$N_{dof} \propto h^{-\dim} \quad (23)$$

335 where \dim is the dimensionality of the domain (here, $\dim = 2$). Hence, a second-
336 order convergence rate will translate into the error ε_h being linearly proportional
337 to $1/N_{dof}$.

338 5.2.1. Distorted Quadrilateral Meshes

339 A convergence study is performed using four types of quadrilateral grids:
340 uniform, Sinusoidal (with $\zeta = 0.15$), Shestakov mesh (with $a = 0.25$), and Z-
341 mesh (with $s = 0.05$). For the Sinusoidal, Shestakov, and Z-mesh types, a series
342 of embedded grids of increasing resolution is utilized (this is actually part of the
343 standard construction process for these grids). For the random quadrilateral

344 grids, we have simply generated one realization of a grid per refinement level.
 345 In Fig. 8, we show the 2×2 , 8×8 , 32×32 , and 128×128 Shestakov grids
 346 used here. In Fig. 9, we show the 2×2 , 8×8 , 32×32 , and 128×128 random
 347 grids used here.

348 The variation of the L_2 norm of the error as a function of the number of
 349 unknowns rate is graphed in Fig. 10 for quadrilateral grids. A slope of one
 350 is observed for all meshes except for Shestakov meshes. Thus, PWLD finite
 351 element discretization is second-order accurate for most quadrilateral meshes,
 352 even the ones with a significant amount of distortion, and exhibit reduced rates
 353 for highly distorted Shestakov meshes. To further analyze this observation,
 354 we provide the convergence rates for Shestakov and Z meshes in Fig. 11 as a
 355 function of the randomness parameter a (Shestakov meshes) and the skewness
 356 parameter s (Z meshes); recall that $0 \leq a, s \leq 0.5$ and that a value of 0.5 cor-
 357 respond to a structured rectangular grid and a value of close to 0 corresponds
 358 to a severely distorted/skewed grid. For $0.3 \leq a \leq 0.5$, PWLD retains second-
 359 order convergence on Shestakov grids but drastically loses such a rate for more
 360 distorted grids; this is not surprising and we are not aware of any spatial dis-
 361 cretization technique able to preserve second-order convergence on such grids.
 362 For Z-meshes, second-order convergence is retained for all grids, even the highly
 363 skewed grid with $s = 0.05$ (shown in Fig. 12(e), for instance).

364 Finally, Fig. 12 presents some representative quadrilateral grids and the
 365 solution isolines (15 isolines, equally spaced by 0.125 in solution magnitude).
 366 The grids and isolines are not provided for the highest resolution data point
 367 found in Fig. 10 (but the third-to-last data point) so as to display the mesh
 368 effects (at higher grid resolutions, the grid imprints are no longer discernible).

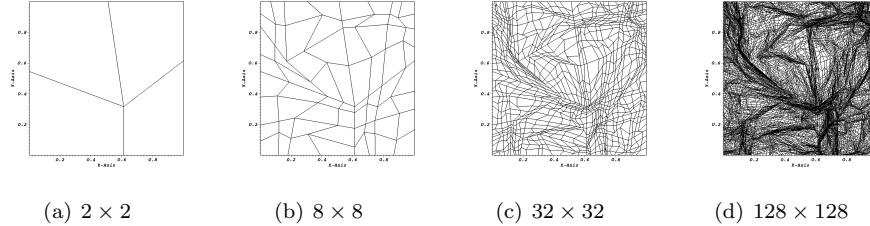


Figure 8: Quadrilateral Shestakov Grids ($a = 0.25$)

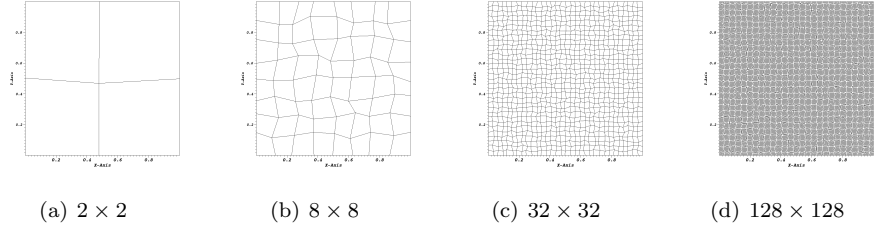


Figure 9: Quadrilateral Random Grids

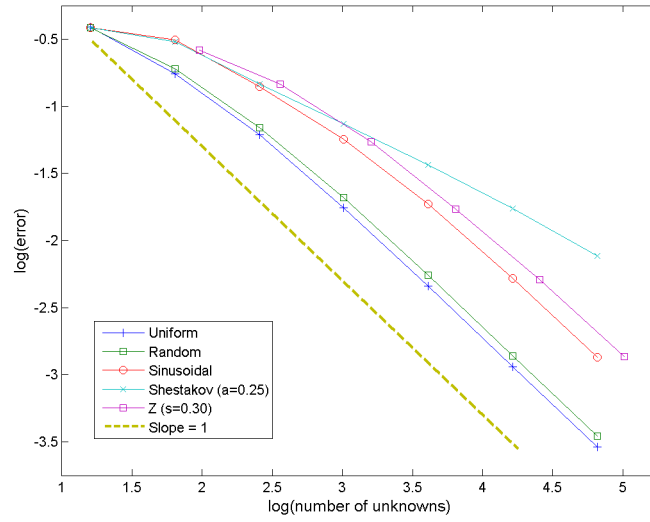


Figure 10: Convergence Study Using Quadrilateral Grids

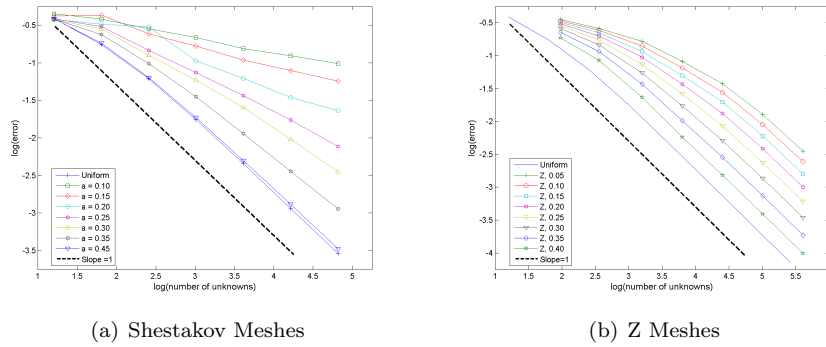


Figure 11: Convergence Rates for Shestakov and Z Quadrilateral Grids as a function of the randomness parameter a (Shestakov) and the skewness parameter s (Z)

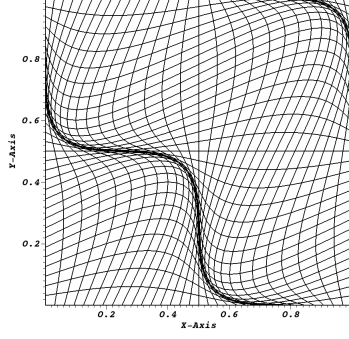
5.2.2. Polygonal Meshes

We carry out the same study as in the previous Section but using polygonal grids this time. We employ the same terminology (random, sinusoidal, Shestakov, Z) to denote the polygonal meshes generated. However, recall that this denomination only describes the manner in which the vertices (used as input for the bounded Voronoi diagram) have been obtained. Fig. 13 shows the convergence rate study on polygonal grids. Second-order accuracy is observed for all grids, including the Shestakov grids generated with $a = 0.15$ and $a = 0.25$, and a Z-mesh obtained with a skewness coefficient of $s = 0.05$. Table 3 summarizes the types and number of polygonal cells used for the highest resolution point in Fig. 13. For instance, The percentages of cells that are not triangular nor quadrangular for the random, Sinusoidal, Z-mesh, and Shestakov polygonal grids are 87%, 94%, 58%, and 82%, respectively.

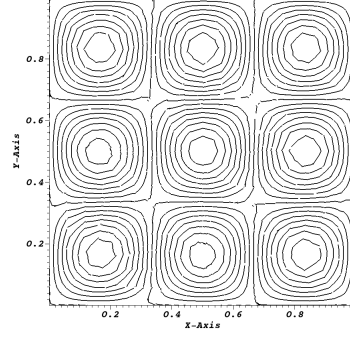
Finally, Fig. 14 presents some representative polygonal grids and the solution isolines (15 isolines, equally spaced by 0.125 in solution magnitude). The grids and isolines are not provided for the highest resolution data point of Fig. 13 so as to display more prominently some mesh effects (at increased resolutions, the grid imprints are no longer discernible).

Polygon type	Random	Sinusoidal	Z-mesh	Shestakov
Triangle	50	0	0	58
Quadrangle	489	231	2732	665
Pentagon	1080	588	696	1090
Hexagon	1299	2878	2585	1107
Heptagon	851	424	478	724
Octagon	351	104	40	363
Nonagon	79	0	10	154
Decagon	20	0	6	42
Hendecagon	5	0	4	14
Dodecagon	1	0	4	5
13 sides	0	0	2	2
14 sides	0	0	2	0
17 sides	0	0	0	1
22 sides	0	0	2	0

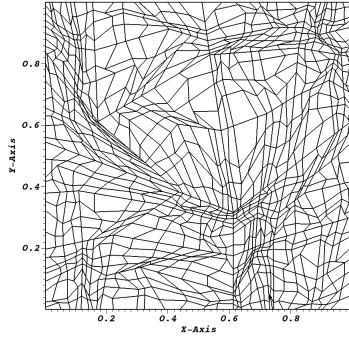
Table 3: Number and type of polygonal cells shown in Fig. 13



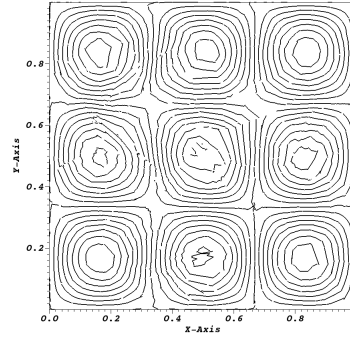
(a) 32×32 Sinusoidal ($\zeta = 0.15$), Mesh



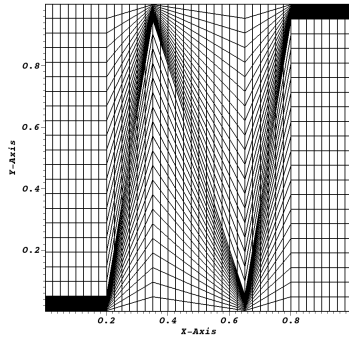
(b) 32×32 Sinusoidal ($\zeta = 0.15$), Isolines



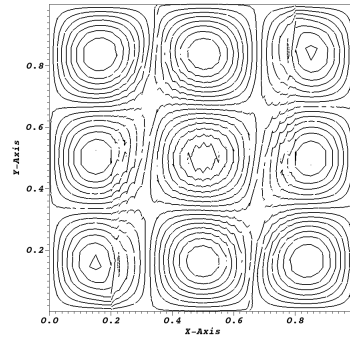
(c) 32×32 Shestakov ($a = 0.25$), Mesh



(d) 32×32 Shestakov ($a = 0.25$), Isolines



(e) 40×40 Z-mesh ($s = 0.05$), Mesh



(f) 40×40 Z-mesh ($s = 0.05$), Isolines

Figure 12: Quadrilateral Grids and Solution isolines

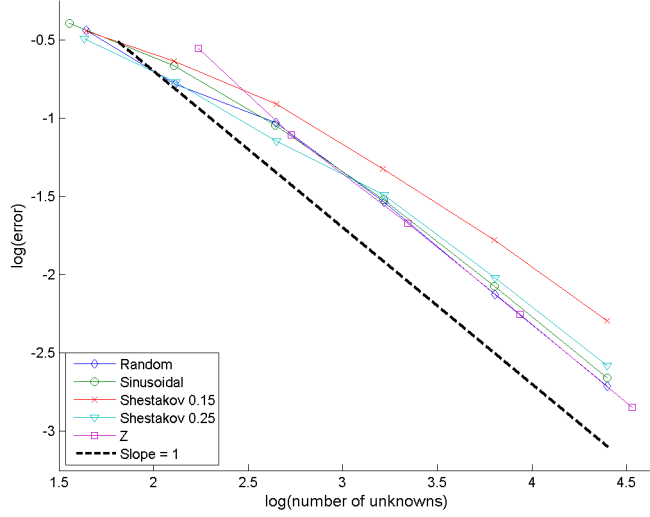


Figure 13: Convergence Study Using Polygonal Grids

5.3. Tensor Diffusion Tests Using Polygonal Grids

In this series of run, we replace the traditional diffusion coefficient with a full symmetry tensor,

$$D \longrightarrow \mathbb{D}. \quad (24)$$

In our numerical experiments, we use

$$\mathbb{D} = \begin{bmatrix} (x+1)^2 + y^2 & -xy \\ -xy & (x+1)^2 \end{bmatrix}, \quad (25)$$

as found in the test cases carried out for mimetic finite differences on polygonal grids in [3, 4]. The exact solution is again given by Eq. (20) with $\nu = 3$ on a unit square domain. With mimetic finite differences, the spatially varying coefficients and tensors are evaluated at the center of mass of the cells, whereas in our finite element discretization, they are evaluated at quadrature points. Specifically, the following changes were made to accommodate for the diffusion tensor: (1) the element stiffness matrix is now

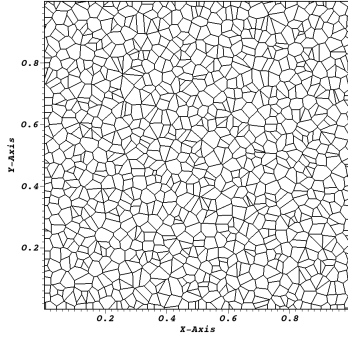
$$(\mathbb{D}^{xx} \partial_x E + \mathbb{D}^{xy} \partial_y E) \partial_x b + (\mathbb{D}^{yx} \partial_x E + \mathbb{D}^{yy} \partial_y E) \partial_y b, \quad (26)$$

as it should be; (2) the integrand of the line integrals is modified as follows

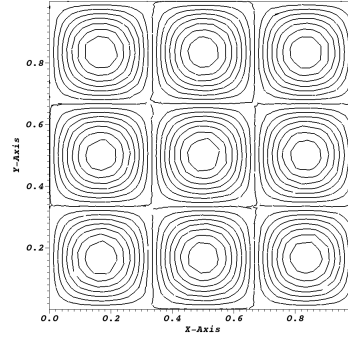
$$D \partial_n E b = D \vec{\nabla} E \cdot \vec{n} b \longrightarrow \mathbb{D} \vec{\nabla} E \cdot \vec{n} b; \quad (27)$$

and, (3) the diffusion coefficient appearing in the penalty factor is replaced with the largest eigenvalue of the diffusion tensor at the edge's midpoint

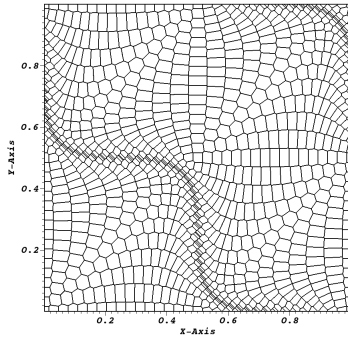
$$\frac{C}{2} \left(\frac{D^+}{h_\perp^+} + \frac{D^-}{h_\perp^-} \right) \longrightarrow \frac{C}{2} \left(\frac{\|\mathbb{D}\|_2^+}{h_\perp^+} + \frac{\|\mathbb{D}\|_2^-}{h_\perp^-} \right), \quad (28)$$



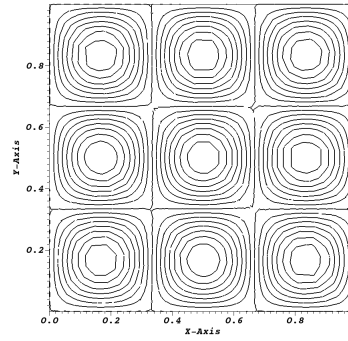
(a) Random Mesh (6374 N_{dof})



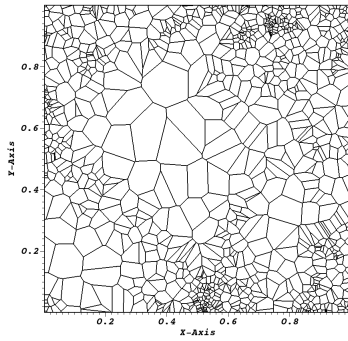
(b) Random Mesh Isolines



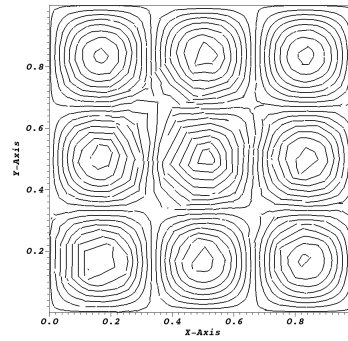
(c) Sinusoidal Mesh (6332 N_{dof})



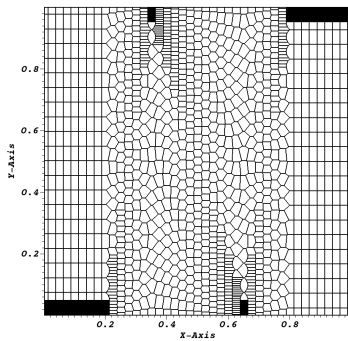
(d) Sinusoidal Mesh Isolines



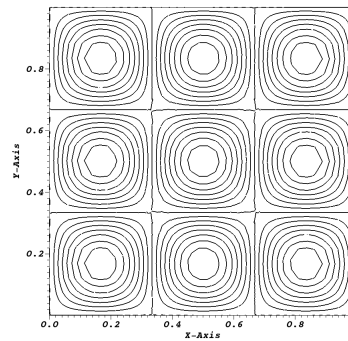
(e) Shestakov ($a = 0.10$) Mesh (6317 N_{dof})



(f) Shestakov Mesh Isolines



(g) Z-mesh ($s = 0.05$) (8644 N_{dof})



(h) Z-mesh Isolines

401 (we could have computed the largest eigenvalue of \mathbb{D} at every quadrature point
 402 appearing in the edge integrals of the penalty term, but choosing the midpoint
 403 value avoids doing this while preserving second-order convergence).
 404 The same polygonal grids as in Section 5.2.2 are used to study the con-
 405 vergence of the PWLD discretization for the tensor diffusion problem. Fig. 15
 406 presents the convergence rates for these polygonal grids. Again, second-order
 407 accuracy is observed for all grids, including the Shestakov grids generated with
 408 $a = 0.15$, and a Z-mesh obtained with a skewness coefficient of $s = 0.05$.

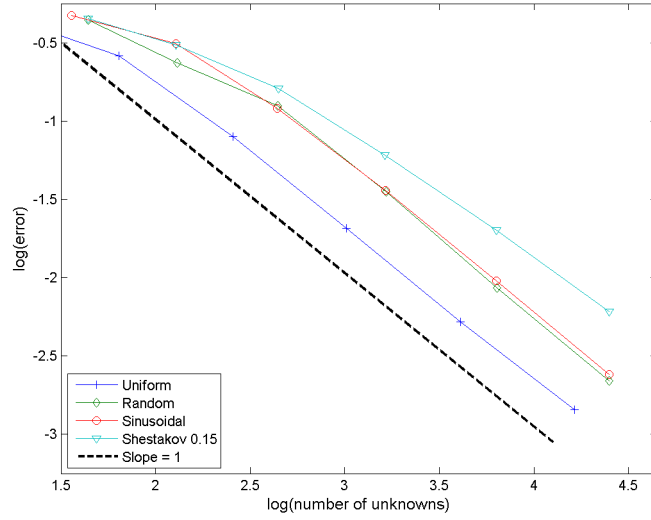


Figure 15: Rate of Convergence for the Tensor Diffusion Problem Using Polygonal Grids

409 5.4. Adaptive Mesh Refinement Using PWLD Finite Elements

In this Section, we use the PWLD discretization to seamlessly handle AMR
 grids and compare the rate of convergence rate of AMR grids with the ones of
 uniformly refined grids. In the AMR process, the cells whose error is within
 20% of the maximum detected error are flagged for refinement, that is, a value
 of $\theta = 0.8$ is employed in Eq. (16). To compare the numerical errors and obtain
 the rate of convergence, we employ again the method of manufactured solutions.
 This time, a rapidly spatially varying function is chosen as the exact solution:

$$\begin{aligned}
 E^{exa}(x, y) &= 100 \frac{xy(L_x - x)(L_y - y)}{(L_x L_y)^2} \exp\left(-\frac{(x - x_0)^2 + (y - y_0)^2}{\varsigma}\right) \\
 &\quad \text{in } \mathcal{D} = [0, L_x] \times [0, L_y]. \quad (29)
 \end{aligned}$$

410 We have chosen the location of the peak to be $x_0 = \frac{6}{10}L_x$, $y_0 = \frac{7}{10}L_y$, with $\varsigma =$
 411 $L_x L_y / 100$. The diffusion coefficient and absorption cross section are $D = 1/6$

412 and $\sigma_a = 1$. This exact solution satisfies zero-Dirichlet boundary conditions.
 413 One then can compute the corresponding volumetric source term $Q(x, y)$ used
 414 to generate the right-hand of the discrete linear system. We solve the radiation
 415 diffusion equation on a sequence of grids with increasing resolution. The
 416 coarsest grid level uses simply a 2×2 grid with quadrangles. This initial grid is
 417 either uniformly refined or locally adapted using the refinement criteria set forth
 418 in Section 4. The L_2 -norm of the error (difference between the exact and the
 419 computed numerical solutions) is plotted in Fig. 16. As expected, both refine-
 420 ment strategies lead to a convergence rate of one measured against the number
 421 of unknowns, demonstrating the second-order accuracy of PWLD discretization
 422 on both grid types. We note that when using an AMR strategy the solution is
 423 obtained with roughly a savings of a factor of 5 to 6 in terms of the number of
 424 unknowns. The numerical solution obtained with AMR is graphed on Fig. 17.
 425 Fig. 18 shows the AMR grids at cycles 5, 10, 15, and 20. The location of peak in
 426 the exact solution is locally refined as the number of adaptivity cycles increases.
 427 Fig. 18(d) presents a zoom on the AMR grid of cycle 15 where one can note
 428 the presences of several (degenerated) octogonal cells surrounded by once-more
 429 refined neighbors on all of their sides. Since these cells possess eight unknowns
 430 with the PWLD discretization, as opposed to only four with a standard bilinear
 431 discontinuous discretization, the 3-irregular rule of Bank does not need to be
 432 applied. Table 4 provides the types and number of polygonal cells used in the
 433 last AMR grid.

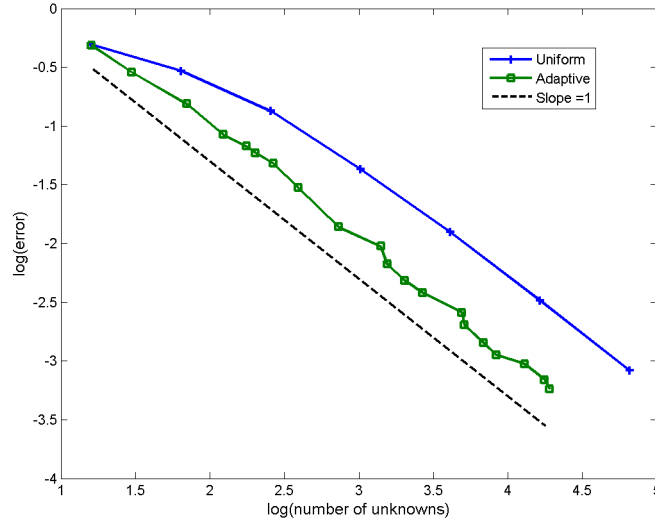


Figure 16: Rate of Convergence Using Uniform and Locally Adapted Grids

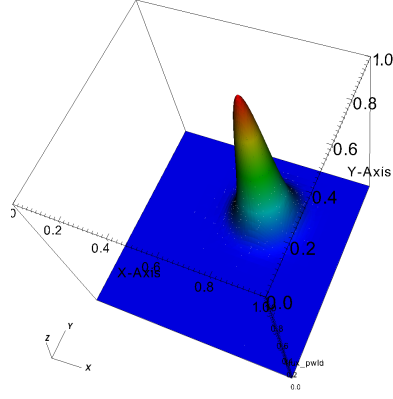
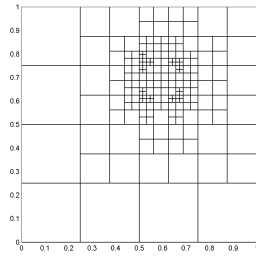
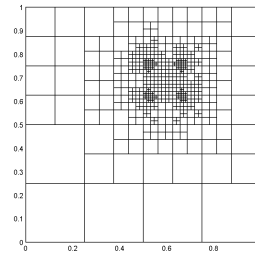


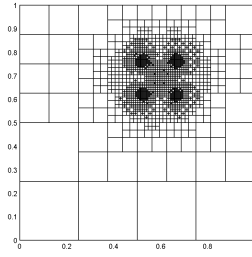
Figure 17: Numerical solution at the last adaptivity cycle



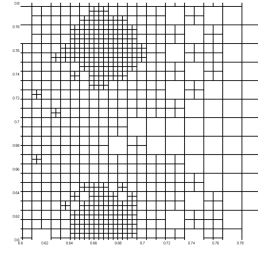
(a) Cycle # 5



(b) Cycle # 10



(c) Cycle # 15



(d) Zoom (Cycle # 15)

Figure 18: AMR Grids at various adaptivity cycles

Quadrangle	8297
Pentagon	446
Hexagon	227
Heptagon	56
Octagon	98

Table 4: Number and type of polygonal cells at adaptivity cycle # 20

434 6. Conclusions

435 A piece-wise linear discontinuous (PWLD) finite element discretization has
436 been applied to the radiation diffusion equation on arbitrary polygonal grids.
437 The Symmetric Interior Penalty stabilization technique has been employed and
438 extended to polygonal cells. The resulting linear system is SPD and can be
439 effectively solved using PCG. Second-order convergence has been numerically
440 verified on highly distorted grids. Polygonal grids have been generated from
441 bounded Voronoi diagrams created using vertex locations from severely dis-
442 torted quadrilateral grids; many meshes contain polygons with a high number
443 of vertices (e.g., > 6).

444 One of the attractive features of a PWL discretization lies in its handling of
445 locally refined grids. Cells adjacent to more refined cells do not possess hanging
446 nodes on the common edges with the refined cells but rather the nature of
447 the coarse cell is changed to that of a polygon with additional sides. We have
448 fully embedded this characteristic of PWL finite elements within an automated
449 adaptive mesh refinement process and verified that second-order convergence
450 was retained while reducing the number of unknowns for the same level of
451 accuracy when compared with uniformly refined quadrilateral grids.

452 This paper shows that the radiation diffusion equation can be effectively
453 discretized on arbitrary polygonal meshes using a piece-wise linear discontinuous
454 finite element approximation. This will allow us to use proven DFEM-based
455 DSA preconditioners [23] to tackle radiation transport problems on polygonal
456 grids in the future and will be the topic of subsequent publications.

457 Acknowledgments

458 The author is grateful to Dr. Alex Shestakov (LLNL) for providing Refer-
459 ence [36] and for suggesting studying smooth meshes (Sinusoidal grids) as well.
460 We would also like to acknowledge Dr. Michael Hall (LANL) for retrieving a
461 Fortran77 copy of the “Shestakov” program.

References

- [1] Wachspress. *A Rationale Finite Element Basis*. New York : Academic Press, 1975.
- [2] Todd S. Palmer. Discretizing the diffusion equation on unstructured polygonal meshes in two dimensions. *Annals of Nuclear Energy*, 28(18):1851 – 1880, 2001.
- [3] Y. Kuznetsov, K. Lipnikov, and M. Shashkov. The mimetic finite difference method on polygonal meshes for diffusion-type problems. *Computational Geosciences*, 8:301–324, 2004.
- [4] Franco Brezzi, Konstantin Lipnikov, and Valeria Simoncini. A Family of Mimetic Finite Difference Methods on Polygonal and Polyhedral Meshes. *Math. Models Methods Appl. Sci.*, 15(10):1533–1551, 2005.
- [5] Konstantin Lipnikov, Mikhail Shashkov, and Daniil Svyatskiy. The mimetic finite difference discretization of diffusion problem on unstructured polyhedral meshes. *Journal of Computational Physics*, 211(2):473 – 491, 2006.
- [6] Teresa S. Bailey. *The piecewise linear discontinuous finite element method applied to the RZ and XYZ transport equations*. PhD thesis, Texas A&M University, 2008.
- [7] Teresa S. Bailey, Marvin L. Adams, Brian Yang, and Michael R. Zika. A piecewise linear finite elements discretization of the diffusion equation for arbitrary polyhedral grids. *Journal of Computational Physics*, 227:3738–3757, 2008.
- [8] K. Lipnikov and M. Shashkov. A framework for developing a mimetic tensor artificial viscosity for lagrangian hydrocodes on arbitrary polygonal meshes. *Journal of Computational Physics*, 229(20):7911 – 7941, 2010.
- [9] T. S. Palmer. Unstructured polyhedral mesh thermal radiation diffusion. *American Nuclear Society Winter Meeting*, Nov. 12-16 2000. Washington, DC.
- [10] J. Hyman, J. Morel, M. Shashkov, and S. Steinberg. Mimetic finite difference methods for diffusion equations. *Computational Geosciences*, 6:333–352, 2002.
- [11] J.E. Morel, Randy M. Roberts, and Mikhail J. Shashkov. A local support-operators diffusion discretization scheme for quadrilateral r-z meshes. *Journal of Computational Physics*, 144(1):17 – 51, 1998.
- [12] J.E. Morel, Michael L. Hall, and Mikhail J. Shashkov. A Local Support-Operators Diffusion Discretization Scheme for Hexahedral Meshes. *Journal of Computational Physics*, 170(1):338 – 372, 2001.

- 499 [13] D. N. Arnold. An interior penalty finite element method with discontinuous
500 elements. *SIAM J. Numer. Anal.*, 19:742–760, 1982.
- 501 [14] Douglas N. Arnold, Franco Brezzi, Bernardo Cockburn, and L. Donatella
502 Marini. Unified analysis of discontinuous galerkin methods for elliptic prob-
503 lems. *SIAM J. Numer. Anal.*, 39(5):1749–1779, 2002.
- 504 [15] G. Kanschat. *Discontinuous Galerkin Methods for Viscous Incompressible*
505 *Flow*. Advances in Numerical Mathematics. Teubner Research, Wiesbaden,
506 Germany, 2007.
- 507 [16] Marvin L. Adams and Edward W. Larsen. Fast iterative methods for
508 discrete-ordinates particle transport calculations. *Progress in Nuclear En-*
509 *ergy*, 40:3–159, 2002.
- 510 [17] James S. Warsa, Todd A. Wareing, and Jim E. Morel. Krylov iterative
511 methods and the degraded effectiveness of diffusion synthetic acceleration
512 for multidimensional S_N calculations in problems with material disconti-
513 nuities. *Nucl. Sci. Eng.*, 147:218–248, 2004.
- 514 [18] Todd A. Wareing, John M. McGhee, Jim E. Morel, and Shawn D. Pautz.
515 Discontinuous finite element S_N methods on three-dimensional unstruc-
516 tured grids. *Nucl. Sci. Eng.*, 138:256–268, 2001.
- 517 [19] James S. Warsa. A Continuous Finite Element-Based, Discontinuous Fi-
518 nite Element Method for Sn Transport. *Nuclear Science and Engineering*,
519 160:385–400, 2008.
- 520 [20] Yaqi Wang and Jean C. Ragusa. On the convergence of dgfm applied to
521 the discrete ordinates transport equation for structured and unstructured
522 triangular meshes. *Nuclear Science and Engineering*, 163:56–72, 2009.
- 523 [21] Teresa S. Bailey, James S. Warsa, Jae H. Chang, and Marvin L. Adams. A
524 Piecewise Bi-Linear Finite Element Spatial Discretization of the S_n Trans-
525 port Equation. *International Conference on Mathematics and Computa-*
526 *tional Methods Applied to Nuclear Science and Engineering*, May 8-12 2011.
527 Rio de Janeiro, Brazil.
- 528 [22] Yaqi Wang and Jean C. Ragusa. Standard and goal-oriented adaptive mesh
529 refinement applied to radiation transport on 2d unstructured triangular
530 meshes. *Journal of Computational Physics*, 230:763–788, 2011.
- 531 [23] Yaqi Wang and Jean C. Ragusa. Diffusion synthetic acceleration for high-
532 order discontinuous finite element S_N transport schemes and application
533 to locally refined unstructured meshes. *Nuclear Science and Engineering*,
534 166:145–166, 2010.
- 535 [24] R. V. Garimella. Mstk: A flexible infrastructure library for developing
536 mesh-based applications. In *Proceedings of the 13th International Meshing*
537 *Roundtable*, Williamsburg, VA., 2004.

- [25] CGAL, Computational Geometry Algorithms Library.
http://www.cgal.org.
- [26] Geert-Jan Giezeman and Wieger Wesselink. 2D polygons. In *CGAL User and Reference Manual*. CGAL Editorial Board, 4.2 edition, 2013.
http://www.cgal.org/Manual/4.2/doc_html/cgal_manual/packages.html#Pkg:Polygon2.
- [27] J.L. Lions. Problemes aux limites non homogenes a donnees irregulieres. In JacquesLouis Lions, editor, *Numerical Analysis of Partial Differential Equations*, volume 44 of *C.I.M.E. Summer Schools*, pages 283–292. Springer Berlin Heidelberg, 2011.
- [28] J. Nitsche. Über ein Variationsprinzip zur Lösung von Dirichlet-Problemen bei der Verwendung von Teilräumen, die keinen Randbedingungen unterworfen sind. *Abh. Math. Univ. Hamburg*, 36:9–15, 1971.
- [29] Bruno Turcksin. *Acceleration Techniques For Discrete-Ordinates Transport Methods With Highly Forward-Peaked Scattering*. PhD thesis, Texas A&M University, 2012.
- [30] M. Ainsworth and J. T. Oden. *A posteriori Error Estimation in Finite Element Analysis*. John Wiley & Sons, New York, NY, 2000.
- [31] Tobias Leicht and Ralf Hartmann. Anisotropic mesh refinement for discontinuous galerkin methods in two-dimensional aerodynamic flow simulations. *International Journal for Numerical Methods in Fluids*, 56(11):2111–2138, 2008.
- [32] R.E. Bank. An efficient implementation of local mesh refinement algorithms. In J.E. Flaherty I. Babuka, J. Chandra, editor, *Adaptive Computational Methods for Partial Differential Equations*, pages 74–81. SIAM, Philadelphia, PA, 1983.
- [33] J.E Morel, J.E Dendy Jr., Michael L Hall, and Stephen W White. A cell-centered lagrangian-mesh diffusion differencing scheme. *Journal of Computational Physics*, 103(2):286 – 299, 1992.
- [34] David S Kershaw. Differencing of the diffusion equation in lagrangian hydrodynamic codes. *Journal of Computational Physics*, 39(2):375 – 395, 1981.
- [35] A.I Shestakov, J.A Harte, and D.S Kershaw. Solution of the diffusion equation by finite elements in lagrangian hydrodynamic codes. *Journal of Computational Physics*, 76(2):385 – 413, 1988.
- [36] A. Shestakov, D. Kershaw, and G. Zimmerman. Test problems in radiative transfer calculations. *Nuclear Science and Engineering*, 105:88–104, 1990.
- [37] Yvan Notay. An Aggregation-Based Algebraic Multigrid Met. *Electronic Transactions on Numerical Analysis*, 37:123–146, 2010.

- 576 [38] Mikhail Shashkov and Stanly Steinberg. Solving diffusion equations with
577 rough coefficients in rough grids. *Journal of Computational Physics*,
578 129(2):383 – 405, 1996.
- 579 [39] Patrick J. Roache. *Fundamentals of Verification and Validation*. Hermosa
580 Publishers, September, 2009.

Compressed File of Latex files

[Click here to download Compressed File of Latex files: submission.zip](#)